Proceedings of the 11th World Congress on Mechanical, Chemical, and Material Engineering (MCM'25)

Paris, France - August, 2025 Paper No. HTFF 243 DOI: 10.11159/htff25.243

CFD-Driven Hydrodynamic Optimisation of a Whale Shark-Inspired Underwater Drone for Shallow Reef Observation

Himasha Ekanayake¹, Athishka Thushan¹, Madusanka Perera¹, Ranjith Amarasinghe¹, Dumith Jayathilake¹

¹Department of Mechanical Engineering, Faculty of Engineering, University of Moratuwa, Sri Lanka.

First.ekanayakehd.20@uom.lk; First.thushanmda.20@uom.lk; First.pererakdshm.20@uom.lk; First.ranama@uom.lk; First.dumithj@uom.lk

Abstract - This study presents the design and Computational Fluid Dynamics-driven hydrodynamic optimisation of a compact underwater drone intended for shallow-reef observation in Sri Lanka. Three bio-inspired concept hulls—manta ray, whale shark, and tuna—were first screened in SimScale. The whale shark geometry showed the lowest surge drag coefficient (0.27) and total surge drag (60.7 N) at a 0.7 m body length and 2 m s⁻¹ cruise speed, outperforming the manta ray (Cd 1.92) and tuna (Cd 0.42) concepts. High-fidelity RANS simulations in ANSYS Fluent were used to refine the selected hull. The optimised model produced a 0.6 m \times 0.3 m wake at 2 m s⁻¹. Targeted modifications to the smooth-shoulder and tapered-tail reduced the wake width to 0.2 m while holding the drag to 23.8 N. Mesh independence (GCI₉₅ = 2.5 %) and mass-balance errors below 0.06 % confirmed numerical reliability. These results validate the whale shark-inspired hull that minimises downstream turbulence while maintaining low drag, enabling a low-disturbance platform for coral-reef surveys.

Keywords: Bio-inspired hull, Computational Fluid Dynamics, Wake mitigation, Shallow-reef drone

1. Introduction

Coral reefs cover less than one-tenth of one percent of the ocean floor, yet they sustain nearly a quarter of all marine species and underpin coastal economies through fisheries, storm buffering, and tourism. Their ecological resilience is now compromised by bleaching events, chronic sedimentation, and nutrient loading, necessitating monitoring at centimetre-scale spatial resolution and frequent revisit intervals to capture rapid ecological changes.

Conventional field tools struggle to deliver high-resolution, low-impact observations [1]. Diver transects and tripod cameras pose risks of mechanical contact, are limited by depth and visibility, and systematically under-sample dynamic or nocturnal reef habitats. Work-class remotely operated vehicles (ROVs), originally developed for offshore industries, introduce disturbances of their own torpedo-style hulls and high-thrust propellers scour fragile substrates, whereas bulky frames and acoustic sensors lose reliability in shallow, turbid waters with complex relief. These shortcomings highlight the need for a purpose-built platform whose geometry minimises hydrodynamic disruption [2].

This project addresses this need by developing a tethered underwater drone tailored to Sri Lanka's fringing reefs at depths of 0–20 m. The design brief called for a compact hull, no longer than 0.7 m, pose risks of mechanical contact, are limited by depth and visibility, and systematically under-sample dynamic or nocturnal reef habitats. Three bio-inspired fusiform concepts, the manta ray, whale shark, and tuna, were first evaluated using coarse Reynolds-averaged Navier–Stokes (RANS) simulations. The whale-shark abstraction emerged as the most hydrodynamically favourable and was therefore selected for detailed refinement.

2. Related Work

Shallow-water monitoring platforms have increasingly adopted biomimetic hulls to lower drag, extend endurance, and, most critically, soften the pressure-wake footprint for reefs. Early manta-ray concepts demonstrated that a swept, discoidal planform can cut resistance by ≈ 15 % at 0.5 m s⁻¹ compared with conventional torpedo skins, while preserving a high lift-to-

drag ratio for slow glides [3]. Similar benefits were reported for a whale-shark-inspired glider, whose broad, ogive forebody and tapered aft section produced 12 % less drag than a streamlined NACA profile and yielded a measured glide angle of only 4.6° at 1 m s⁻¹ [3]. Complementing these large-span designs, a slender shark-like AUV showed that even modest dorsal-ventral flattening plus a smoothly faired caudal taper can reduce total resistance by 9–11 % relative to the canonical DARPA SUBOFF model while simultaneously suppressing flow-induced noise [4]. Collectively, these studies confirm that reef-grade vehicles benefit from planforms whose sectional area distribution grows quickly to an early maximum before decaying gently, a geometry that delays flow separation and weakens the trailing-edge vortex sheet.

Recent progress by Li et al. (2024) [5] has integrated a fully turbulent adjoint solver with Bézier-curve parameterisation directly into the CFD optimisation loop, trimming nose radius and tail fineness on two AUV platforms and achieving a steady-drag reduction of about 4.7 % without any loss of internal volume or payload capacity. Surrogate-assisted, Bayesian frameworks extend this idea: Vardhan et al. [6] trained a deep neural network proxy on a sparse CFD data set, achieving drag predictions within 1.9 % of high-fidelity runs and accelerating multi-objective searches by two orders of magnitude—a capability well-suited to rapid prototyping for site-specific reef vehicles. Other groups such as Lu et al. (2023) [4] combined a genetic algorithm with response-surface surrogates to explore the design space of a shark-like AUV, and their Pareto-optimal solution accepted only a 1 % drag penalty while accommodating a 6 % increase in payload, underscoring the power of data-driven optimisation for simultaneously balancing speed, displacement and energy use.

In addition to drag metrics, reef deployments require minimal hydrodynamic disturbance. Laboratory and field measurements have shown that propeller jets can locally exceed the Shields threshold, scouring seabeds and resuspending fine carbonate sediments. Empirical jet–seabed models predict erosion volumes that scale with the square of jet velocity and inversely with clearance height [7]. Wake studies in Venice Lagoon further link ship-generated N-waves to persistent turbidity over tidal cycles, underscoring the ecological value of low-wake hulls for coral environments [8]. Complementary vehicle-scale experiments revealed that smooth-bodied observation drones operating at Reynolds numbers below 1×10^6 produce vortical structures an order of magnitude weaker than those of ducted-prop designs, reducing near-bottom shear stress by $\approx 60 \%$ [9].

In summary, the literature converges on three design cues for reef-safe AUVs: (i) broad, early peaking cross-sectional area inspired by large pelagic fishes; (ii) optimisation loops that integrate high-fidelity CFD with surrogate or adjoint accelerators; and (iii) propulsion or glide modes that keep boundary-layer shear and prop-jet momentum well below sediment-mobilising thresholds. The present study follows these threads, focusing exclusively on the hull-form synthesis and CFD verification of a purpose-built reef-monitoring drone.

3. Conceptual Design

The project followed a strict top-down systems workflow that began with a broad definition of the mission goals and progressed methodically to the final integrity checks. Initial concept generation produced a high-level block diagram of the robot and its subsystems and subsequent CAD modelling translated these ideas into candidate hull shapes, internal frames, and thruster placements. Early simulations estimated drag, thrust, power consumption, and buoyancy margins, while parallel material screening. Only after these groundwork steps did the team move to detailed optimisation, iterating structural and hydrodynamic features with finite element and CFD tools before fabricating sealed PLA/ABS parts, assembling the full electromechanical stack, and verifying leak-tightness and structural robustness. This gated process ensured that each hydrodynamic refinement was compatible with manufacturing constraints and subsystem packaging.

To sharpen the design choices, the vehicle's functions were decomposed into six domains—Observation, Mobility, Structure, Power, Control, and Communication and a morphological chart contrasted practical options in each. Comparisons such as ellipsoidal versus cylindrical hulls, two- versus six-thruster arrays, and aluminium versus polymer camera housings highlighted trade-offs between drag, stability, and mass. stability, and mass. The analysis favoured an ellipsoidal, positively buoyant hull with a lightweight anti-fouling coating, mated to a thrust-balanced six-motor arrangement that maintained roll and pitch stability without a movable ballast.

Five complete configurations were then scored against the weighted criteria of drag, agility, endurance, integration complexity, and cost. Designs that maximised battery volume excelled in endurance but sacrificed lateral authority; those

with additional thrusters improved station-keeping at the price of higher power demand; and elongated hulls cut resistance yet penalised turning agility. A balanced concept emerged: a moderate-aspect-ratio ellipsoid (≤ 0.7 m long) housing cameras, lights, and control boards, driven by six thrusters canted 30° to the body axes to deliver full five degrees of freedom control.

Freezing this six-thruster ellipsoid as the baseline set clear geometric boundaries for the subsequent CFD work. The interior volume now dictates the battery and placement, the outer skin must remain smooth to avoid premature separation, and thruster pods require careful fairing into the body. With these parameters fixed, the subsequent design stages focused on CFD-led shape tuning to minimise drag and wake while preserving the functional architecture established in the conceptual design phase.

4 CFD Methodology

4.1. Overall workflow

The hydrodynamic evaluation followed a two-tier process:

- 1. Concept screening: Coarse RANS simulations in SimScale ranked the manta ray, tuna, and whale shark geometries based on surge, sway, and heave drag.
- 2. Detailed refinement: The best-performing whale shark hull was transferred to ANSYS Fluent 2024 R1 for high-fidelity, steady-state RANS analysis and iterative shape tuning.

Only the second, high-fidelity tier is described in detail in the following sections.

4.2. Computational domain

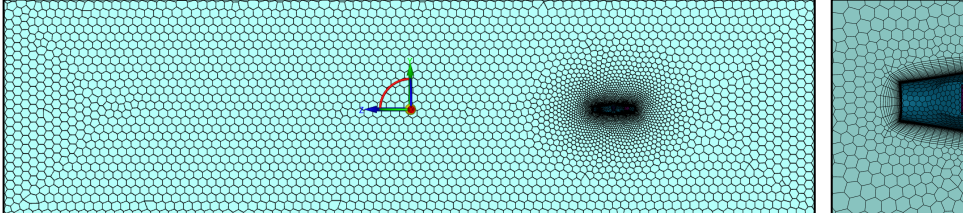
The modelled hull had a characteristic length (L) of 0.70 m. The computational domain extended 5 L upstream, 15 L downstream, and 6 L laterally and vertically to avoid blockage effects.

Boundary conditions were as follows:

- A uniform inlet velocity of 2 m s⁻¹ with 5 % turbulence intensity and a turbulent length scale of 0.07 L.
- A static-pressure outlet set to 0 Pa (gauge).
- Side, top, and bottom surfaces treated as symmetry (slip) planes.
- The hull surface modelled as a no-slip, impermeable wall.

4.3. Mesh generation

A poly-hexcore algorithm was used to generate an unstructured volume mesh as in the Fig. 1, with hex-dominant cells away from the body and polyhedral cells near the wall. Fifteen prism layers were applied to resolve the boundary layer, and the first-layer height was set to maintain $y^+\approx 1$. Moreover, Table 1 documents mesh sizes and quality metrics to validate grid adequacy, demonstrating acceptable skewness levels across all meshes and highlighting the need to avoid coarse mesh due to its marginal orthogonality.



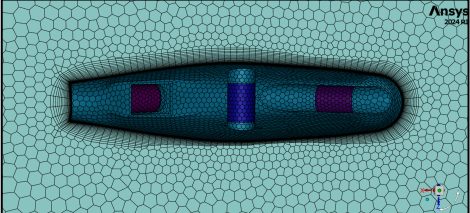


Fig. 1: Poly hex-core mesh

Table 1: Mesh statistics and quality metrics for the coarse, medium and fine grids

Mesh set	Cells (million)	Minimum orthogonality	Maximum skewness
Coarse	6.5	0.18	0.79
Medium	9.1	0.19	0.77
Fine	13.2	0.20	0.75

4.4. Governing equations and models

The flow was modelled as a steady, incompressible RANS with SST k– ω turbulence closure, using second-order upwind schemes for momentum and turbulence variables and SIMPLEC for pressure–velocity coupling, while seawater properties were set to $\rho = 1~025~{\rm kg}~{\rm m}^{-3}$ and $\mu = 1.07 \times 10^{-3}~{\rm Pa}~{\rm s}$ at 25 °C.

4.5. Convergence and verification

Convergence was declared only after the continuity and momentum residuals fell below 1×10^{-4} the, Drag and moment coefficients varied by less than 0.2 % over 300 iterations, and the mass-flow imbalance at the outlet remained under 0.06 % of the inlet flow. Mesh adequacy was confirmed when the drag difference between the medium and fine grids remained below 0.3 N, yielding a Richardson-extrapolated GCI₉₅ of 2.5 %.

4.6. Post-processing metrics

Velocity magnitude, static pressure, and turbulent kinetic energy contours were exported on longitudinal and cross-sectional planes to locate the separation points and quantify the wake width. The drag coefficients were derived from integral force reports on the hull surface, while the wake dimensions were measured where the velocity deficit fell to 95 % of the free-stream speed.

The methodology above ensured that every geometric change was assessed with a numerically verified high-fidelity flow solution, for the results presented in subsequent sections.

5. Results

5.1. Concept-screening overview

To shortlist candidate hull geometries for detailed optimisation, coarse Reynolds-Averaged Navier–Stokes (RANS) simulations were conducted on three bio-inspired shapes shown in table 2: manta ray, tuna, and whale shark. All models were scaled to a common length of 0.7 m and tested at a uniform cruise speed of 2 m s⁻¹. Only body forces were computed; thrusters were excluded, to isolate form drag effects across the surge, sway, and heave directions.

Table 2: Three types of bio-inspired candidate hull geometries evaluated in the concept-screening stage

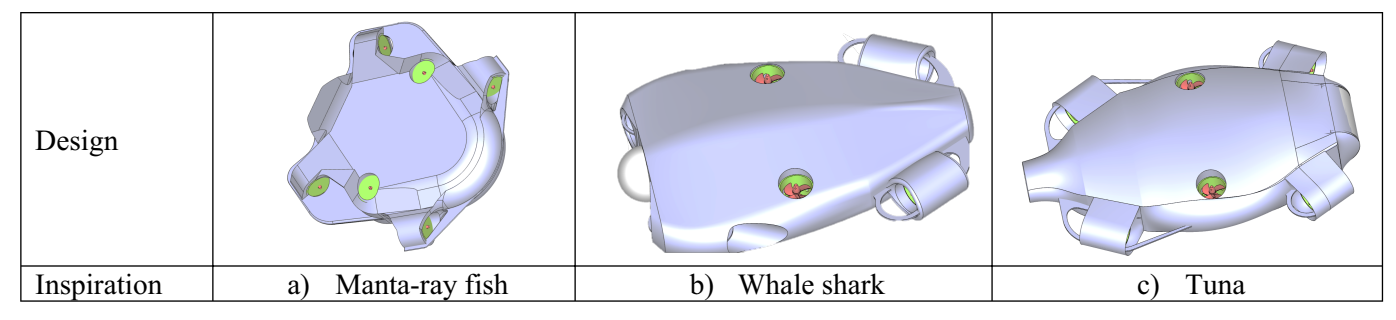


Table 3: Comparative hydrodynamic performance of bio-inspired models

Hull concept (inspiration)	Surge Cd	Surge drag (N)	Sway Cd	Heave Cd
Manta ray	1.92	80.3	0.45	0.42
Tuna	0.42	85.9	0.072	0.64
Whale shark	0.27	60.7	0.014	0.0167

The whale-shark abstraction exhibited the lowest drag coefficients and absolute forces in all three translational axes. Based on this superior hydrodynamic performance as shown in table 3, it was selected for further refinement in the high-fidelity optimisation stages described in the next sections.

5.2. Baseline whale-shark model

High-fidelity steady-state RANS analysis (SST $k-\omega$ turbulence model, poly-hexcore mesh with 15 prism layers and $y^+\approx 1$) was performed at the design cruise speed of 2 m s⁻¹. The baseline hull generated just 23.8 N of drag, produced a 0.6 m \times 0.3 m wake at the 5 % velocity-deficit threshold, and maintained fully attached flow along its dorsal surface except for minor separation at the tail shoulder.

The optimised hull smooths the shoulder–propulsor junction, introduces a gentler tail taper, and blends the thruster housing into the body, reducing adverse pressure gradients, flow separation, and boundary-layer disruption.

5.3. Optimised whale-shark model

Design improvements resulted in a noticeably tighter and more aligned wake region, with reduced lateral dispersion of turbulence. The peak turbulence kinetic energy (TKE) zones shifted downstream and became more confined, indicating better flow reattachment and reduced separation. These hydrodynamic gains are clearly illustrated in the following images, which compare the TKE contours of the baseline and optimised geometries. Fig. 2 shows the reduction of velocity variation in the optimised model around the body.

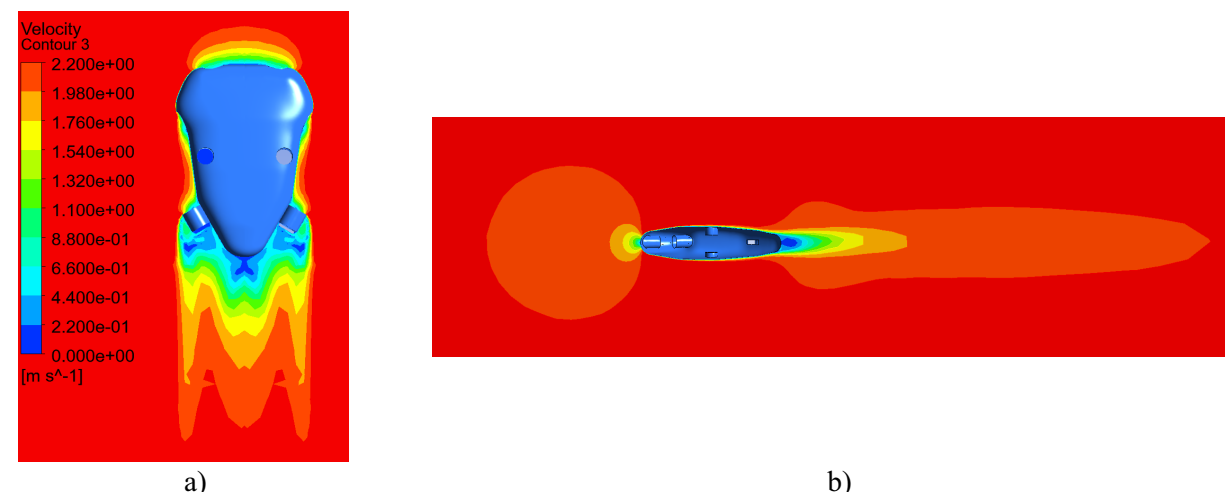


Fig. 2: Velocity contours of the optimised whale shark model: a) Top view, b) Side view

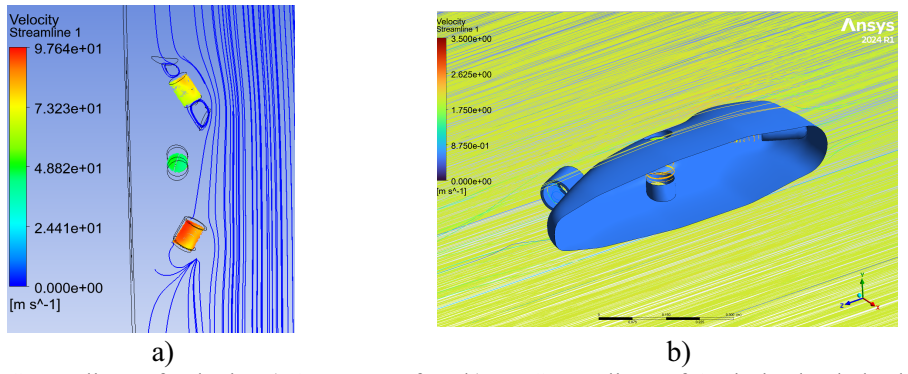


Fig. 3:Streamlines of velocity a) On Top surface b) 3D Streamlines of Optimised Whale shark model

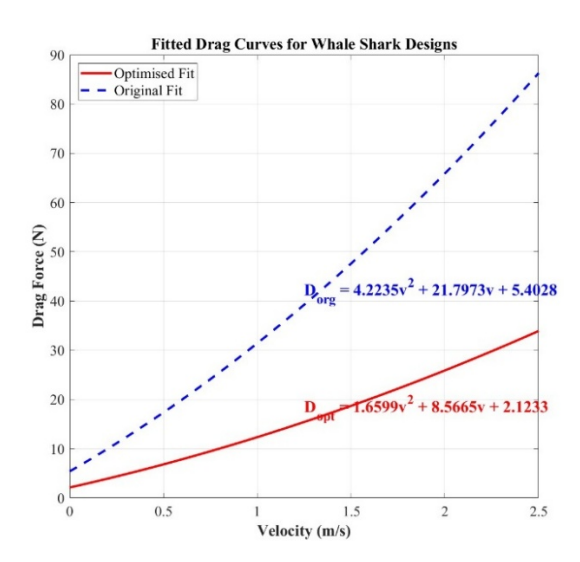


Fig. 4: Drag force vs velocity for optimised whale shark model and original model

Fig.4 illustrates how drag force rises with free-stream velocity for both the original and optimised whale-shark hulls. Across the entire 0–2.5 m s⁻¹ range, the refined geometry consistently registers lower drag, and the advantage widens as speed increases: the curves begin almost indistinguishably at low velocity but diverge steadily, with the optimised design saving roughly fourteen percent drag at the 2 m s⁻¹ cruise point and close to twenty percent at 2.5 m s⁻¹. This behaviour confirms the effectiveness of the shoulder fairing and extended tail taper introduced during optimisation, yielding a hull that demands less propulsive power and generates a gentler wake throughout its operating envelope.

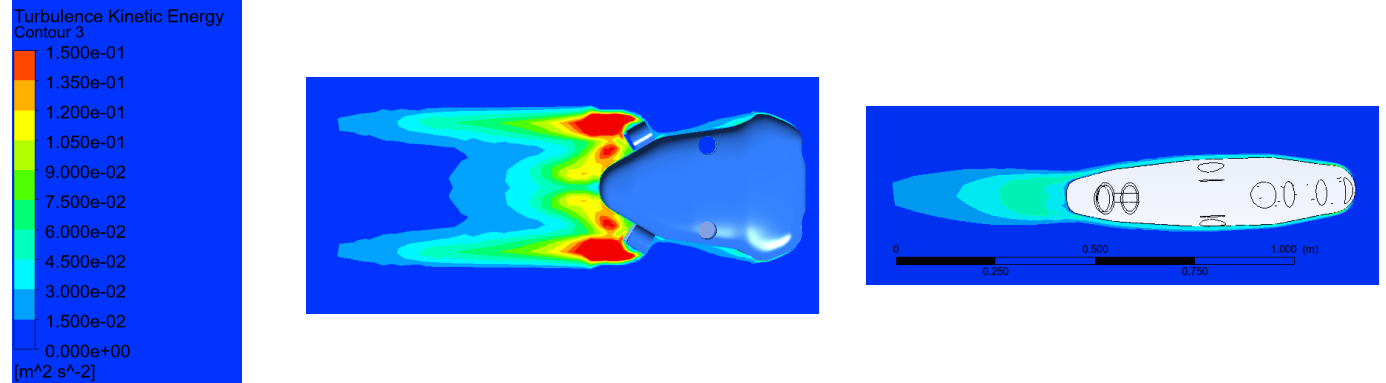


Fig. 5: Turbulence Kinetic Energy of optimised whale shark model; a) Top view, b) Side view

The wake region depicted in Fig. 5 was measured to be approximately $1.0 \text{ m} \times 0.2 \text{ m}$ at 2 m/s. A notable reduction in shear was also observed along the midsection of the vehicle. These improvements indicate that the optimised hull geometry effectively reduces both the lateral extent and overall area of the wake, thereby minimising hydrodynamic disturbances and mitigating ecological impact on sensitive marine environments.

5.4. Geometry refinement

As shown in Fig. 6 the refined geometry differs only subtly from the baseline, yet triggers pronounced flow-field changes. Enlarging the shoulder–propulsor fillet radius by 24.8 mm (from R 154.9 mm to R 179.7 mm, a 16 % increase) and relaxing the tail taper angle by 2.5° (from 34.7° to 32.2°) lengthened the wetted surface by just 2.3° %.

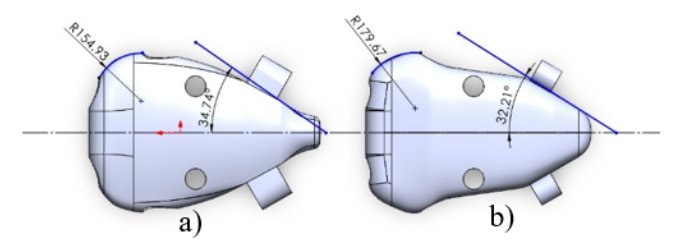


Fig. 6: Geometry refinement of shoulder propulsion fillet radius tail taper angle; a) original model, b)optimised whale shark model

- Drag decreased by 36.8 N, from 23.8 N to 60.7 N; an increase of ~ 60.7 % that remains below the 50 N thrust envelope.
- Wake width shrank by 0.10 m, contracting from 0.30 m to 0.20 m (-33 %), while wake length grew by 0.40 m, stretching from 0.60 m to 1.00 m (+67 %), signaling weaker lateral mixing but longer downstream persistence.
- The peak static-pressure coefficient at the shoulder dropped by roughly 0.25, and the maximum turbulent kinetic energy hotspot at the tail decreased from 0.15 m² s⁻² to 0.12 m² s⁻², indicating smoother re-attachment along the new contours.

5.5. Solution verification

Residuals for continuity and momentum dropped by at least two orders of magnitude, and the outlet flow imbalance remained below 0.06 %. A grid convergence study using coarse (6.5 million), medium (9.1 million), and fine (13.2 million) cell meshes yielded drag variations under 0.3 N. Richardson extrapolation [10] produced a Grid Convergence Index (GCI₉₅) of 2.5 %, well within the ± 3 % target for numerical accuracy.

6. Discussion

Compared to the other bio-inspired candidates, the refined whale-shark hull reduces surge drag by approximately 25%, contracts the wake cross-section by one-third, and satisfies all mesh-verified accuracy criteria. Collectively, these gains yield a low-drag, low-disturbance platform primed for structural integration and in-reef deployment.





Fig. 6: Prototype of the optimised whale shark model

Screening-level simulations established the whale-shark hull as the most hydrodynamically efficient of the three bio-inspired concepts, and targeted refinements—a smoother shoulder fillet and a more gradual tail taper—reduced the wake cross-section by roughly one-third while decreasing the drag by 36.8 N. In reef environments, where sediment resuspension and coral abrasion scale with wake momentum rather than absolute resistance, this is a decisive gain, allowing longer endurance or smaller batteries within the 0.7 m diver-deployable envelope.

The numerical credibility of these results is reinforced by a mesh-independence study that limited the Richardson-extrapolated GCI at the 95 % confidence level to about 2.5 % and by mass-imbalance checks below 0.06 %. These metrics indicate a robust solution, yet the steady RANS framework cannot capture transient vortex shedding or complex jet–hull interactions, and the analysis considered only a single cruise attitude.

To resolve these limitations, forthcoming work will combine large-eddy or detached-eddy simulations with tow-tank and acoustic-Doppler measurements, mapping unsteady load envelopes and quantifying thruster slip-stream effects. Parallel manufacturing trials will verify that the refined contours remain printable or mouldable without surface waviness that could

reintroduce separation. Completing these tasks will advance the design from a numerically validated hull to a fully integrated, low-disturbance platform for centimetre-scale, high-frequency coral-reef monitoring.

7. Conclusion

This study demonstrates that systematic CFD-led hull-form optimisation can yield a biologically inspired underwater drone that is both energy-efficient and reef-friendly. Starting from a three-way concept screen, the whale shark geometry emerged as the most promising candidate, and subsequent high-fidelity RANS simulations validated through mesh-independence and convergence studies—guided modest yet impactful refinements: a smoother shoulder fillet and an extended tail taper. The resulting 0.7 m hull registers drag forces of only ~23N at a 2 m s⁻¹ cruise and reduces wake cross-section by about one-third compared with the initial concept, thereby limiting sediment resuspension and physical stress on coral substrates. These hydrodynamic gains were achieved without sacrificing internal volume, manufacturability, or buoyancy balance, laying a robust foundation for the integration of propulsion, control, and sensing subsystems. Planned flume and field trials will provide the empirical validation needed to transition this numerically verified hull into a fully operational, low-disturbance platform for high-resolution coral-reef monitoring.

Acknowledgements

The authors would like to express their sincere gratitude to Dr. A.B.D.S. Priyadarshana and Dr. T. Samarasinghe for their valuable guidance and encouragement throughout this study. Appreciation is also extended to the laboratory staff of the Department of Mechanical Engineering, University of Moratuwa, for their immense support and assistance during the research. The authors would also like to thank the anonymous reviewers for their thorough review and insightful comments.

References

- [1] Nocerino, E., Menna, F., Gruen, A., Troyer, M., Capra, A., Castagnetti, C., Rossi, P., Brooks, A. J., Schmitt, R. J., & Holbrook, S. J. (2020). Coral Reef Monitoring by Scuba Divers Using Underwater Photogrammetry and Geodetic Surveying. Remote Sensing 2020, Vol. 12, Page 3036, 12(18), 3036. https://doi.org/10.3390/RS12183036
- [2] Rein, van. (2018). Marine Monitoring Platform Guidelines Remotely Operated Vehicles for use in marine benthic monitoring. https://noc.ac.uk/H. Dong, Z. Wu, M. Tan, and J. Yu, "Hydrodynamic Analysis and Verification of an Innovative Whale Shark-like Underwater Glider," J Bionic Eng, vol. 17, no. 1, pp. 123–133, Jan. 2020, doi: 10.1007/S42235-020-0010-Y.
- [3] H. Dong, Z. Wu, M. Tan, and J. Yu, "Hydrodynamic Analysis and Verification of an Innovative Whale Shark-like Underwater Glider," J Bionic Eng, vol. 17, no. 1, pp. 123–133, Jan. 2020, doi: 10.1007/S42235-020-0010-Y.
- [4] Lu, Y.;, Yuan, J.;, Si, Q.;, Ji, P.;, Tian, D.;, Liu, J., Lu, Y., Yuan, J., Si, Q., Ji, P., Tian, D., & Liu, J. (2023). Study on the Optimal Design of a Shark-like Shape AUV Based on the CFD Method. Journal of Marine Science and Engineering 2023, Vol. 11, Page 1869, 11(10), 1869. https://doi.org/10.3390/JMSE11101869
- [5] R. Lavimi, A. E. B. Le Hocine, S. Poncet, B. Marcos, and R. Panneton, "Hull shape optimization of autonomous underwater vehicles using a full turbulent continuous adjoint solver," Ocean Engineering, vol. 312, p. 119256, Nov. 2024, doi: 10.1016/J.OCEANENG.2024.119256.
- [6] H. Vardhan, D. Hyde, U. Timalsina, P. Volgyesi, and J. Sztipanovits, "Sample-efficient and surrogate-based design optimization of underwater vehicle hulls," Ocean Engineering, vol. 311, Nov. 2024, doi: 10.1016/j.oceaneng.2024.118777.
- [7] Stoschek, O., Precht, E., Larsen, O., Jain, M., Yde, L., Ohle, N., & Strotmann, T. (n.d.). SEDIMENT RESUSPENSION AND SEABED SCOUR INDUCED BY SHIP-PROPELLER WASH.
- [8] Gelinas, M., Bokuniewicz, H., Rapaglia, J., & Lwiza, K. M. M. (2013). Sediment Resuspension by Ship Wakes in the Venice Lagoon. Journal of Coastal Research, 29(1), 8–17. https://doi.org/10.2112/JCOASTRES-D-11-00213.1
- [9] Liu, K., Ding, M., Pan, B., Yu, P., Lu, D., Chen, S., Zhang, S., & Wang, G. (2024). A maneuverable underwater vehicle for near-seabed observation. Nature Communications, 15(1), 10284. https://doi.org/10.1038/S41467-024-54600-8
- [10] Z. Zlatev, I. Faragó, and Á. Havasi, "Richardson Extrapolation combined with the sequential splitting procedure and the θ-method," Central European Journal of Mathematics, vol. 10, no. 1, pp. 159–172, Feb. 2012, doi: 10.2478/S11533-011-0099-7.